Chinese Journal of
POLYMER SCIENCE

RESEARCH ARTICLE

https://doi.org/10.1007/s10118-026-3642-5
Chinese J. Polym. Sci. **2026**, *44*, 1727–1737

A Transparent Acoustic Damping Hydrogel with Dual-scale Bicontinuous Microphase Separation

Chen-Chen Lou[a], Bao-Hu Wu[b], Sheng-Tong Sun[a*], and Pei-Yi Wu[a*]

[a] *State Key Laboratory of Advanced Fiber Materials, College of Chemistry and Chemical Engineering & Center for Advanced Low-dimension Materials, Donghua University, Shanghai 201620, China*
[b] *Jülich Centre for Neutron Science (JCNS) at Heinz Maier-Leibnitz Zentrum (MLZ) Forschungszentrum Jülich, Garching 85748, Germany*

Electronic Supplementary Information

Abstract Underwater camouflage materials can be hidden either from sight by being transparent or from sound by absorbing acoustic waves, but achieving both in one material remains challenging due to their distinct chemical designs. Here we decouple these conflicting properties using a hierarchically structured hydrogel featuring unique dual-scale bicontinuous microphase separation. By precisely integrating hydrophilic and hydrophobic units, we engineer three intertwined polymer-rich and aqueous phases spanning nano-to-micro length scales. This unique nanoconfinement preserves optical clarity by minimizing light scattering while facilitating ultrahigh broadband energy dissipation. Furthermore, the hydrogel's acoustic impedance matches that of water, maximizing sound wave incidence into the material, where the propagating waves are scattered and attenuated through viscoelastic damping within the highly tortuous hydrophilic phases. A hydrogel film only 4 mm thick can absorb nearly 78% of incident sound energy. These findings highlight molecular-engineered hierarchical phase separation as a powerful strategy for developing advanced opto-acoustic soft materials.

Keywords Hydrogels; Damping materials; Phase separation; Underwater sound absorption

Citation: Lou, C. C.; Wu, B. H.; Sun, S. T.; Wu, P. Y. A transparent acoustic damping hydrogel with dual-scale bicontinuous microphase separation. *Chinese J. Polym. Sci.* **2026**, *44*, 1727–1737.

INTRODUCTION

Underwater vehicles, machines, and devices play vital roles in ocean exploration, marine biology, the offshore industry, and deep-sea reconnaissance.[1–3] A key challenge lies in developing adaptive camouflage materials that are optically invisible to avoid interference with underwater imaging and observation, yet acoustically stealthy to evade sonar detection.[4,5] For example, aquatic robots and drones often incorporate high-resolution cameras for optical reconnaissance, while requiring acoustic absorption for concealment. In such applications, high-performance sound-absorbing materials are of particular interest because of their ability to reduce both the echo intensity and self-generated noise, thereby mitigating detection by active or passive sonars.[6,7] However, traditional transparent window materials such as glass and plexiglass suffer from a significant acoustic impedance mismatch with water and low sound absorption coefficients, making them easily detectable underwater.[7] Current sound-absorbing (meta)materials are typically designed with subwavelength cavity- or particle-doped composite/porous structures to maximize internal acoustic energy dissipation through resonance, scattering, friction, or energy conversion effects.[8–14] Nonetheless, these designs often compromise the optical transparency owing to the inclusion of light-absorbing and scattering components.

Intrinsically viscoelastic soft materials, primarily elastomers and gels, represent promising self-adaptive underwater coatings that may reconcile optical transparency with sound absorption. Acoustic waves are mechanical waves that propagate elastically through a material.[15] At the molecular level, they induce alternating compression and elongation of the polymer chains and segments, dissipating vibrational energy as heat.[16] Thus, enhancing the viscosity-related damping capacity of soft materials can significantly improve their sound absorption properties.[7,17] Moreover, acoustic impedance matching with water is crucial for reducing the reflection of incident sound waves. Although most polymers exhibit acoustic impedance closer to that of water than inorganic materials, even slight mismatches can cause substantial sound reflection at interfaces.[18–21] Consequently, conventional transparent elastomers, such as polydimethylsiloxane (PDMS), fail to effectively attenuate sound waves owing to impedance mismatch and limited damping capacity (Fig. 1a). Although hydrogels offer nearly perfect acoustic impedance

* Corresponding authors, E-mail: shengtongsun@dhu.edu.cn (S.T.S.)
E-mail: wupeiyi@dhu.edu.cn (P.Y.W.)
Special Topic: Functional Gels
Received February 11, 2026; Accepted March 3, 2026; Published online May 12, 2026

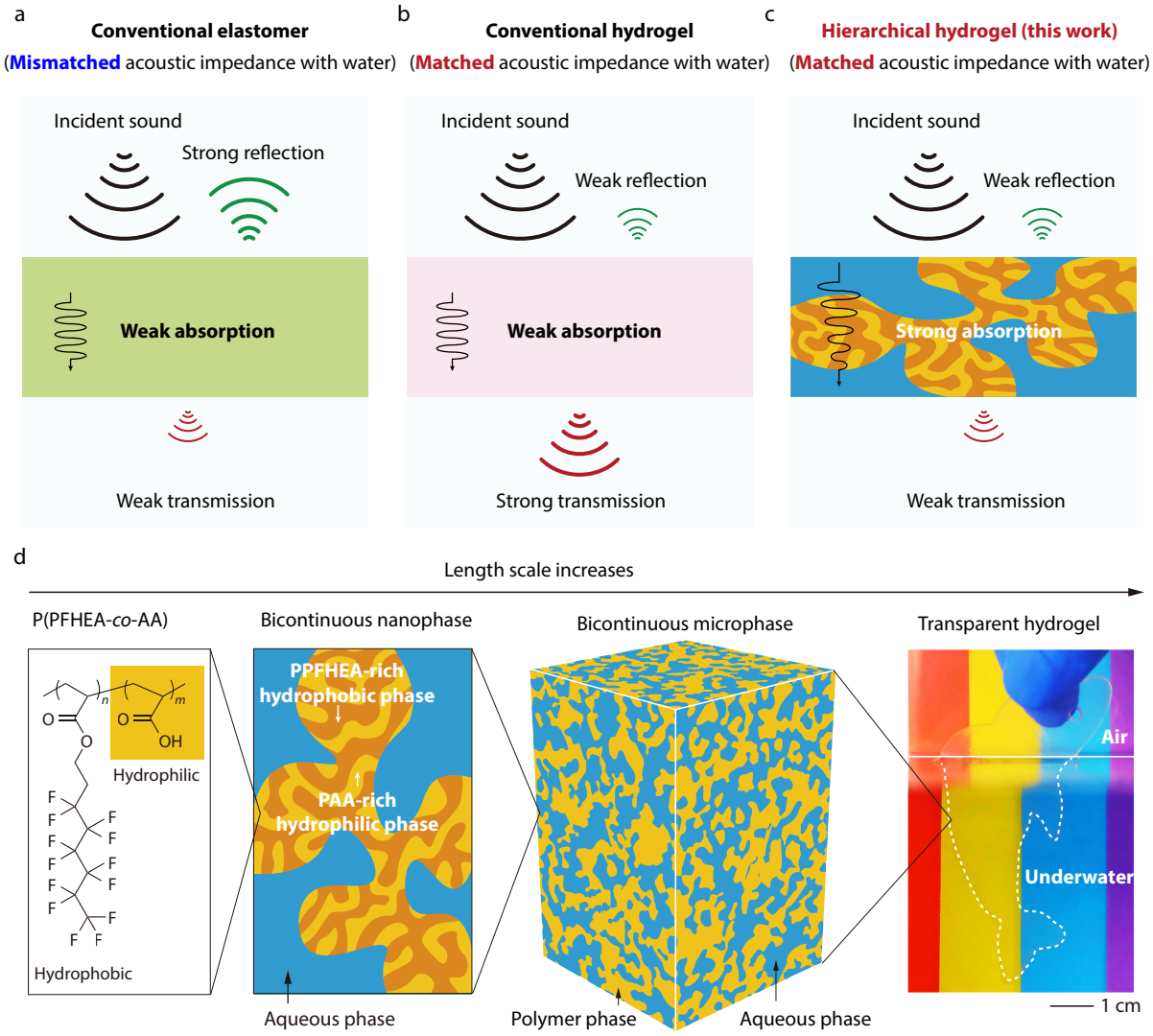

Fig. 1 Schematic design and working mechanism of transparent hierarchical hydrogel for underwater acoustic damping. (a) Conventional transparent elastomers exhibit acoustic impedance mismatch with water, leading to strong sound reflection and weak absorption; (b) Conventional transparent hydrogels have matched acoustic impedance with water but weak damping capacity, resulting in strong sound transmission and weak absorption; (c) Our hierarchical hydrogel integrates matched acoustic impedance with water and high damping capacity, enabling strong sound absorption; (d) Hierarchical structure of P(PFHEA-*co*-AA) hydrogel at different length scales. The right photograph shows the underwater transparency of the P(PFHEA-*co*-$AA_{30\%}$) sample.

matching with water, conventional transparent hydrogels typically possess homogeneous structures and low structural viscosity, leading to similarly weak sound absorption (Fig. 1b). Therefore, hydrogels are often employed as high-sound transmission materials.[3,5,22,23] Phase separation methods have been used to enhance the damping capacity of hydrogels, but the large phase size often sacrifices optical transparency.[24,25] To date, fabricating soft materials that are both optically transparent and acoustically damping remains a formidable challenge.

In this study, we report a novel hierarchically structured hydrogel that combines high optical transparency with broadband acoustic damping capacity (Fig. 1c). Experimentally, the hydrogel was synthesized *via* copolymerization of 2-perfluorohexyl ethyl acrylate (PFHEA) and acrylic acid (AA) (Fig. 1d). Swelling in water induced the formation of a unique bicontinuous structure at both the micro- and nanoscale. At the nanoscale, a PPFHEA-rich hydrophobic phase and a PAA-rich hydrophilic phase form the first level of the bicontinuous structure. At the microscale, the polymer and water phases constituted the second level. We emphasize the importance of this dual-scale bicontinuous nanostructure for acoustic damping because it provides highly tortuous pathways for sound propagation and dissipation through multiple scattering and reflections at phase boundaries.[26,27] Furthermore, owing to the nanoconfined phase separation and a refractive index close to that of water, the hydrogel is fully transparent and nearly invisible in aquatic environments (Fig. 1d). The hydrogel also exhibited acoustic impedance closely matched that of water, maximizing the sound wave incidence. Importantly, the relaxation behavior arising from the hydrogen-bonded PAA-rich hydrophilic phase endows the hydrogel

https://doi.org/10.1007/s10118-026-3642-5

with an ultrahigh damping capacity over a broad underwater sound frequency range (10 Hz–20 MHz; damping figure of merit≈4.2–30.2 MPa). We further elucidate the damping mechanism and demonstrate the potential of this material for underwater acoustic damping and camouflage applications.

EXPERIMENTAL

Materials

2-Perfluorohexylethyl acrylate (PFHEA, Adamas), acrylic acid (AA, TCI), acrylamide (AAm, TCI), 1-hydroxycyclohexyl phenyl ketone (Irgacure 184, TCI), 2-hydroxy-4'-(2-hydroxyethoxy)-2-methylpropiophenone (Irgacure 2959, Adamas), *N*,*N*'-methylenebisacrylamide (MBAA, TCI), NaCl (Macklin), polydimethylsiloxane (PDMS, SYLGARD^{TM} 184 Silicone Elastomer Kit), and artificial seawater (Yier, Seasalt) containing a mixture of dissolved mineral salts. PFHEA and AA were purified by passing through a basic alumina-filled column to remove the inhibitor before use. All other chemicals were used as received.

Preparation of P(PFHEA-*co*-AA) Hydrogel

P(PFHEA-*co*-AA) hydrogels with AA molar fractions varying from 0% to 50% (relative to total monomers) were synthesized *via* photo-induced copolymerization. For a typical synthesis of P(PFHEA-*co*-$AA_{30\%}$), PFHEA (2.78 g, 6.65 mmol) and AA (0.22 g, 2.89 mmol) were mixed with the photoinitiator Irgacure 184 (4.85 mg, 0.25 mol% of total monomers). The mixture was stirred at room temperature for 30 min and sonicated for 20 min to obtain a homogeneous precursor solution. This solution was injected into a glass mold assembled with a release film and silicone spacer of specific thickness. After UV irradiation for 1 h, the P(PFHEA-*co*-$AA_{30\%}$) sample was obtained. The as-prepared sample was then immersed in deionized water at room temperature for three days to reach swelling equilibrium, yielding the final P(PFHEA-*co*-$AA_{30\%}$) hydrogel.

Preparation of PDMS

The PDMS elastomer was prepared using a SYLGARD^{TM} 184 silicone elastomer base and curing agent at a mass ratio of 10:1. The components were mixed and mechanically stirred until uniform, followed by vacuum degassing to remove entrapped air bubbles. The mixture was poured into a silicone mold with a cavity thickness of 4 mm and cured under static conditions at room temperature for 16 h to ensure complete cross-linking.

Preparation of PAAm Hydrogel

Transparent PAAm hydrogel was prepared according to a previously reported procedure for highly entangled hydrogels.[28] Briefly, 30 g of AAm was dissolved in 15 mL of deionized water. Separate solutions of 0.1 mol·mL^{-1} MBAA in water and 0.1 mol·mL^{-1} Irgacure 2959 in ethanol, respectively, were prepared. These solutions were mixed to achieve a molar ratio of water to AAm of 2.0, MBAA to AAm of 1.0×10^{-5}, and Irgacure 2959 to MBAA of 0.4. The precursor solution was sonicated for 3 min at room temperature, injected into a glass mold with a 2-mm-thick silicone spacer, and photopolymerized under UV light for 1 h. The as-prepared PAAm hydrogel was immersed in deionized water for two days to reach swelling equilibrium, yielding a final thickness of about 4 mm.

Characterizations

Tensile and compressive tests were performed using a universal testing machine (UTM2103; Shenzhen Suns Technology). The refractive indices were measured at room temperature using a digital refractometer (PAL-RI, ATAGO) with a built-in yellow light source (589 nm). The transparency of the hydrogel films was evaluated using a UV-Vis spectrophotometer (Lambda 950, PerkinElmer). Low-field $^{1}H/^{19}F$ NMR spectra and 2D correlation spectra were acquired at 20 °C using an NMR analyzer (VTMR20-010V-I, Suzhou Niumag Corporation) equipped with hydrogen and fluorine probes at 20 °C. Atomic force microscopy (AFM) images were obtained using an atomic force microscope (MFP-3D Bio, Oxford Instruments) in tapping mode. Dynamic compression tests at high strain rates were conducted on cylindrical hydrogel samples (diameter is about 20 mm, thickness is about 10 mm) using a ZDSHTB-20/15 Split-Hopkinson pressure bar (SHPB) apparatus. The water content was determined *via* thermogravimetric analysis (TGA, TA Discovery TGA550) under a nitrogen atmosphere, scanning from room temperature to 600 °C at 20 °C·min^{-1}. Differential scanning calorimetry (DSC) measurements were conducted using a differential scanning calorimeter (TA Discovery DSC250) under a nitrogen atmosphere from −30 °C to 50 °C at a heating rate of 20 °C·min^{-1}. DSC samples were sealed in crucibles to prevent water evaporation. The acoustic absorption performance was evaluated using a PVA TePla AM300 scanning acoustic microscope with a 10 MHz transducer to vertically scan a PCB with/without hydrogel coating (thickness is about 4 mm).

Rheological Measurement

Rheological characterization was performed on a HAAKE MARS 60 modular rheometer (Thermo Scientific) with temperature control using 8-mm parallel plates. Frequency sweeps were conducted at a constant strain of 0.1% and set temperatures. Temperature sweeps from −30 °C to 80 °C were performed at 0.1 Hz with a heating rate of 3 °C·min^{-1}. The relaxation spectrum $H(\tau)$ was derived from the frequency-dependent moduli (G' and G'') by solving the following equation:

$$G'(\omega) = \int_{-\infty}^{\infty} H(\tau) \frac{\omega^2\tau^2}{1+\omega^2\tau^2} d\ln(\tau) \quad (1)$$

$$G''(\omega) = \int_{-\infty}^{\infty} H(\tau) \frac{\omega\tau}{1+\omega^2\tau^2} d\ln(\tau) \quad (2)$$

where G' is the storage modulus, G'' is the loss modulus, ω is the angular frequency, τ is the relaxation time (reciprocal of the frequency), and $H(\tau)$ is the relaxation factor.

Small-angle X-Ray Scattering (SAXS)

SAXS experiments were performed using a laboratory-based SAXS-WAXS beamline, KWS-X (XENOCS XUESS 3.0 XL), at JCNS-MLZ, Garching, Germany. A Metal-Jet X-ray source (Excillum D2+) with a liquid metal anode was operated at 70 kV and 3.57 mA, emitting Ga-Kα radiation (λ=1.314 Å). Samples were measured in sealed 2-mm glass capillaries. Temperature-variable experiments used a peltier-controlled stage. The sample-to-detector distance varied from 0.65 m to 1.70 m. SAXS patterns were normalized to an absolute scale, azimuthally averaged to yield 1D intensity profiles, and background-subtracted. The phase separation structure was analyzed using the Power law-Teubner joint model and Beucage model to determine the phase spacing and domain size.

Temperature-variable IR Measurement

Temperature-variable FTIR spectra were acquired on a Nicolet

https://doi.org/10.1007/s10118-026-3642-5

iS50 spectrometer in the transmission mode. A small amount of the precursor solution was deposited between two ZnSe tablets for *in situ* photopolymerization into an ultrathin film. After swelling in water, the hydrated sample was sealed between ZnSe tablets using parafilm. The sample was heated from –20 °C to 80 °C in 2 °C increments at a rate of 1.5 °C·min^{-1}.

Two-dimensional Correlation Spectroscopy (2DCOS)

Temperature-variable FTIR spectra were analyzed using 2D Shige software ver. 1.3 (©Shigeaki Morita, Kwansei Gakuin University, Japan, 2004–2005). In the contour maps, red and blue indicate positive and negative intensities, respectively.

Acoustic Measurements

The underwater acoustic impedance and sound absorption coefficients of the PAAm hydrogel, PDMS, PPFHEA, and P(PFHEA-*co*-AA) hydrogel were measured using the transfer function method with an SW422/SW477 impedance tube system. The tests were conducted in a standard impedance tube filled with deionized water. All the samples were disk-shaped (diameter: 10 cm; thickness: 4 mm) and mounted in a sample holder with sealed edges to prevent water short-circuiting. The sound absorption was measured at room temperature over 0.1–10^9 Hz.

To evaluate the underwater sound wave damping performance, an underwater loudspeaker emitted simulated or real acoustic signals, which were acquired using a Tektronix MDO3024 oscilloscope and an RHS-20 hydrophone. The sample was fixed between the sound source and hydrophone and fully submerged in a water tank.

RESULTS AND DISCUSSION

Synthesis and Optimization of Hierarchical Hydrogel

P(PFHEA-*co*-AA) hydrogels were prepared *via* photo-initiated bulk copolymerization of PFHEA and AA, followed by subsequent swelling in water. AA was selected as the comonomer because of its hydrophilicity and excellent compatibility with PFHEA, which yielded fully transparent precursor solutions (Fig. S1 in the electronic supplementary information, ESI). Fluorinated PPFHEA served as the hydrophobic component because of its high underwater stability and ultralow refractive index.[29,30] To optimize the transparency and damping performance, we varied the AA molar fraction from 0% to 50%. The resulting hydrogels were highly transparent, with >92% transmittance in the visible range when the molar fraction of AA was below 40% (Fig. 2a). This high transmittance implies that the nanodomain size is likely to be below the Rayleigh scattering limit of visible light (generally <40 nm, 1/10 wavelength).[31] Moreover, the refractive index (n) of the representative P(PFHEA-*co*-AA$_{30\%}$) sample is 1.345 (Fig. S2 in ESI), closely matching that of water (n=1.33), and thus contributing to the material's high underwater transparency. Increasing the AA molar fraction to 50% led to large-scale phase separation and a slight reduction in transparency. The water contents of the hydrogels were measured to be relatively low, increasing from 2 wt% for P(PFHEA-*co*-AA$_{10\%}$) to 12.5 wt% for P(PFHEA-*co*-AA$_{50\%}$), indicating a highly confined PAA-rich hydrophilic phase (Fig. S3 in ESI). Despite this low overall water mass content, we continued to classify these materials as hydrogels because water strongly hydrates the PAA-rich phase at high molar concentrations.

Tensile tests revealed that all hydrogels were highly stretchable and tough (Figs. 2b and 2c). The neat PPFHEA exhibited fully elastic behavior, with a Young's modulus of 128 kPa and an elongation of 1508%. Introducing H-bonded AA units significantly stiffened the hydrogel and induced yielding. The optimal mechanical properties were observed for P(PFHEA-*co*-AA$_{30\%}$), with a Young's modulus of 7.2 MPa and toughness of 5.0 MJ·m^{-3}. Further increasing the AA molar fraction gradually reduced the mechanical strength as the higher proportion of soft PAA-rich and aqueous phases began to counterbalance the stiffness imparted by the PPFHEA-rich phase.

Damping refers to the attenuation of vibrations through dissipation of mechanical energy as heat.[32–35] Shear-based rheology provides an indirect yet physically grounded means to assess the acoustic damping capacity, as shear sound waves dissipate more rapidly in viscoelastic media than longitudinal waves.[6,7] Accordingly, we constructed rheological master curves for all hydrogels using the time-temperature superposition principle, with 20 °C as the reference temperature (Fig. 2d). No water-freezing artifacts were observed at low temperatures (from –30 °C to 0 °C), as validated by both the maintained transparency and differential scanning calorimetry (DSC) measurements (Figs. S4 and S5 in ESI). Similar to typical viscoelastic materials, all master curves exhibit three distinct regimes with increasing frequency: rubbery, dissipating (glass transition), and glassy.[33,36] The rheological behavior within the experimental timescale (about 0.1 Hz) reflected the observed mechanical performance, showing a transition from rubbery to dissipating states with increasing AA molar fraction, which is consistent with the tensile results (Fig. S6 in ESI). All master curves displayed a maximum loss factor (tanδ = G''/G'; where G'' and G' are the loss and storage moduli, respectively) peak corresponding to the glass transition of the PPFHEA-rich phase. This peak gradually shifted to lower tanδ values and lower frequencies as the AA molar fraction increased owing to the enhanced nanoconfinement of the hydrophobic network *via* H-bonded AA units.

Notably, the introduction of the AA units also induced a new relaxation peak in the high-frequency regime (1–10^8 Hz). A higher AA molar fraction increased the relative area of this peak compared with that of the PPFHEA-rich phase (from 18% for 10% AA to 75% for 50% AA; Fig. S7 in ESI). We attribute this to the relaxation of the hydrogen-bonded PAA-rich hydrophilic phase. Given that sonar and ultrasonic devices operate between 10 Hz and 20 MHz,[5] this relaxation is critical for high-frequency acoustic damping. Temperature-sweep rheological tests corroborated these characteristics, with the relaxation peak of the PAA-rich phase appearing at low temperatures (Figs. S8 and S9 in ESI). In contrast, the relaxation frequency of the hydrophobic PPFHEA-rich phase falls significantly below the target underwater acoustic band; thus, it contributes negligibly to acoustic damping and primarily maintains structural integrity. While integral to the bicontinuous architecture, the aqueous phase exhibits ultrafast molecular motions with relaxation frequencies far exceeding the acoustic range of interest. Instead, it facilitates acoustic impedance matching and creates tortuous propagation pathways, extending the effective path length of the sound waves within the dissipative phase. Consequently, as sound waves

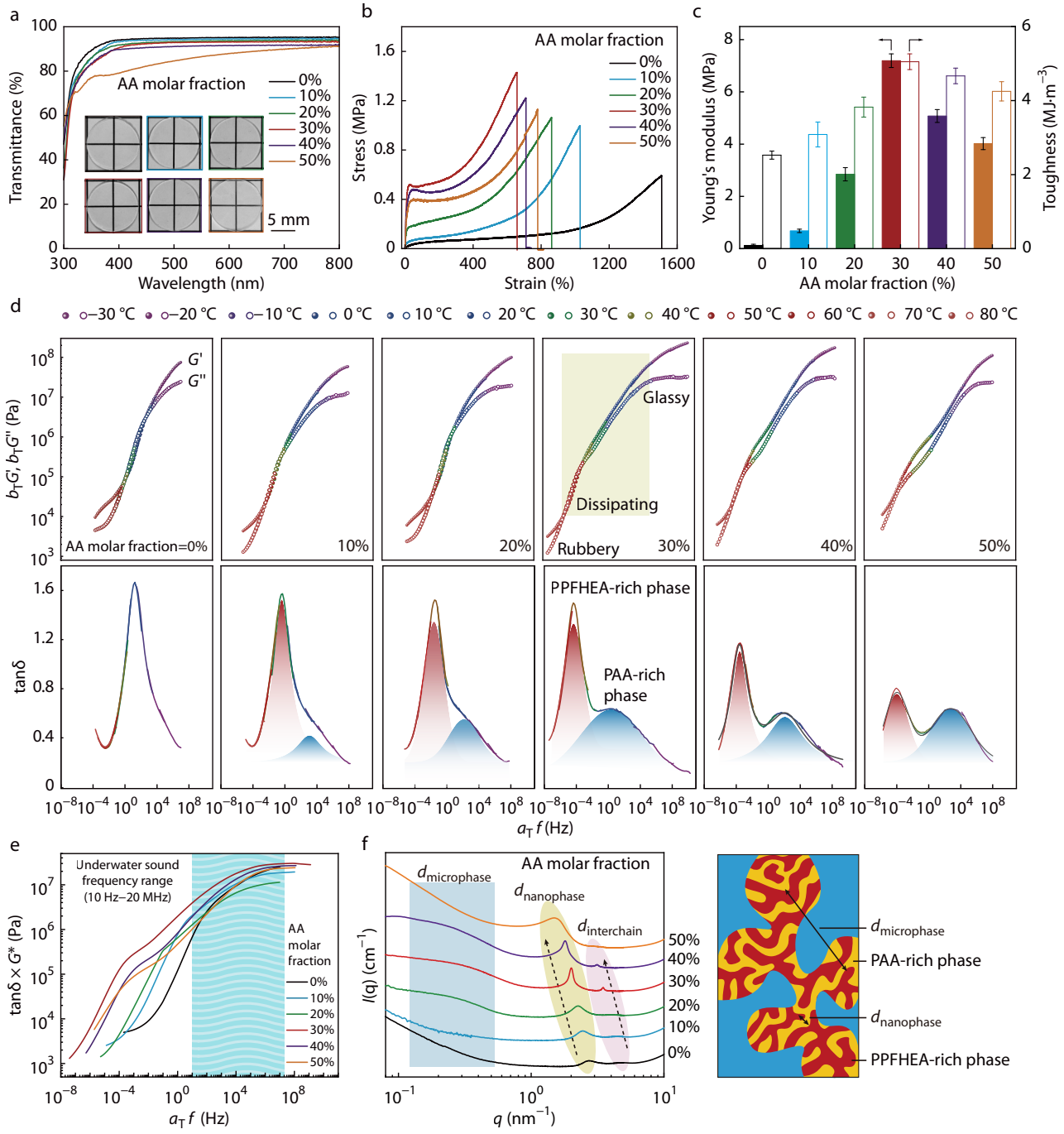

Fig. 2 Mechanical properties and characterization of P(PFHEA-*co*-AA) hydrogels with varying AA molar fractions. (a) Transmittance spectra and corresponding photographs; (b) Tensile stress-strain curves (strain rate: 0.2 s^{-1}); (c) Corresponding Young's moduli and toughness; (d) Time-temperature superposition rheological master curves and corresponding tanδ curves (reference temperature: 20 °C); (e) Damping figure of merits, tanδ × G^*, calculated from (d); (f) Stacked SAXS profiles in log-log scale at 20 °C and schematic hierarchical bicontinuous structure.

propagate through the bicontinuous structure, they undergo repeated phase-boundary crossing, multiple scattering, and mode conversion, ultimately dissipating mechanical energy as heat *via* relaxation of the PAA-rich phase.

To better assess the damping properties from an energetic perspective, we defined the damping figure of merit as tanδ × G^*, where the complex modulus is given by $G^* = \sqrt{(G'^2 + G''^2)}$.[37,38] While the dimensionless loss factor tanδ reflects a material's inherent efficiency in converting mechanical energy into heat, it does not quantify the absolute magnitude of the dissipated energy. By incorporating both dissipative efficiency and structural stiffness, the product tanδ × G^* serves as a more comprehensive figure of merit for the total energy dissipation. A high tanδ × G^* value indicates a superior capacity for attenuating acoustic energy. Across all samples, tanδ × G^* values increased with frequency, demonstrating an en-

hanced damping performance for high-frequency sound waves (Fig. 2e). The P(PFHEA-*co*-$AA_{30\%}$) sample exhibited the highest damping capacity over the entire frequency range. Within the underwater sound frequency range (10 Hz–20 MHz), its damping figure of merit reached 4.2–30.2 MPa, ranking among the highest reported for soft materials.[39–41] Conversion of the master curves into relaxation spectra, which also reflect energy dissipation under dynamic loading[42,43] supported this conclusion (Fig. S10 in ESI). Unless otherwise stated, all subsequent discussions refer to the optimal P(PFHEA-*co*-$AA_{30\%}$) sample. Notably, even after immersion in artificial seawater or various saline solutions (0.2–1 mol·L^{-1} NaCl), the hydrogel maintained a similar swelling ratio as well as high damping capacity (Figs. S11–S14 in ESI), demonstrating its high salt resistance and suitability for both freshwater and marine applications.

The superior damping performance of the P(PFHEA-*co*-$AA_{30\%}$) hydrogel was further validated through dynamic mechanical characterization. Steel ball impact tests were performed to evaluate its response to transient mechanical loads. The hydrogel dissipated impact energy rapidly, achieving an attenuation of approximately 50% of the first-impact force. This performance significantly outperformed both polyacrylamide (PAAm) hydrogel and PDMS controls (Fig. S15 in ESI). Additionally, the mechanical damping capacity under high-speed loading was assessed using a Split-Hopkinson Pressure Bar (SHPB) system. The energy absorption capacity increased sharply from 0.34 MJ·m^{-3} at 500 s^{-1} to 9.05 MJ·m^{-3} at 2000 s^{-1} (Fig. S16 in ESI), demonstrating markedly enhanced energy absorption of the hydrogel at ultrahigh strain rates.

Small-angle X-ray scattering (SAXS) was used to investigate the hierarchical structural evolution of the hydrogels with varying AA molar fractions (Fig. 2f). In the high q region (q>1 nm^{-1}), related to nanostructural features, neat PPFHEA elastomer exhibited two correlation peaks at q≈2.7 and 4.9 nm^{-1}, corresponding to the primary phase-to-phase distance ($d_{nanophase} = 2\pi/q$) and the secondary interchain distance ($d_{interchain}$), respectively. The bicontinuous nanophase separation in the neat PPFHEA elastomer arises from the inherent incompatibility between its hydrocarbon backbone and perfluorinated side chains.[33,44] Incorporating AA units, which are also incompatible with perfluorinated side chains, shifted these peaks to lower q values, indicating an increased interphase and interchain spacing. The samples with 30% and 40% AA exhibited sharper correlation peaks, revealing the formation of a lamellar structure with improved ordering in the bicontinuous nanophase. Further increasing the AA molar fraction to 50% resulted in the disappearance of sharp peaks due to the swelling-induced disruption of the structural order. In the low q region (q<1 nm^{-1}), which reflects microstructural features, no significant microphase separation was observed for neat PPFHEA or the copolymer hydrogel with 10% AA. However, at AA molar fractions of 20%–40%, bicontinuous microphase separation occurred, forming interconnected island-like domains. The average domain spacing ($d_{microphase}$) was approximately 28.6 nm, with domain sizes greater than 15 nm (Fig. S17 in ESI). Further increasing the AA molar fraction to 50% disrupted the bicontinuous microstructure, which was replaced by large aggregates. These SAXS results confirm that the optimal hydrogel with 30% AA possesses a well-developed hierarchical bicontinuous structure at both the micro- and nanoscale.

Dynamic Phase Separation and Physical Interactions

Dual-scale bicontinuous phase separation and internal physical interactions are key structural factors contributing to the high damping performance of the P(PFHEA-*co*-AA) hydrogel. Atomic force microscopy (AFM) phase imaging, which detects phase shifts based on the interaction between the tip and surface, allows the differentiation of phases with distinct viscoelastic properties. Here, AFM clearly revealed the dual-scale bicontinuous structure: aqueous and polymer phases at the microscale (20–100 nm) and PPFHEA-rich and PAA-rich phases at the nanoscale (<10 nm) (Fig. 3a). This three-phase hierarchical structure was further confirmed by two-dimensional low-field ^{1}H nuclear magnetic resonance (NMR) spectroscopy (Fig. 3b). In the 2D low-field NMR spectrum, the T_1/T_2 ratio (T_1: spin-lattice relaxation time; T_2: spin-spin relaxation time) reflects molecular mobility, with a higher ratio indicating lower mobility, and the diagonal line where T_1/T_2=1 represents a fully mobile liquid state.[45,46] Three distinct phases were identified: PPFHEA-rich phase (T_1/T_2=558.8), PAA-rich phase (T_1/T_2=57.1), and aqueous phase (T_1/T_2=14.5). The relatively low T_1/T_2 ratio of the aqueous phase suggests that the water molecules are not strongly confined and can form interconnected tortuous channels for sound propagation. The higher T_1/T_2 ratio of the PPFHEA-rich phase compared to the PAA-rich phase indicates greater confinement of the PPFHEA chains owing to the incorporated H-bonded AA units. This H-bond-induced confinement was also evident in the low-field ^{19}F-NMR spectra with varying AA molar fractions (Fig. S18 in ESI).

Since frequency is not a convenient stimulus for structural analysis, we used temperature as a proxy based on the time-temperature equivalence principle (lower temperature corresponds to shorter time scales or higher frequencies).[43,47] Temperature-variable SAXS was used to study the structural changes from –30 °C to 70 °C, a temperature range employed for time-temperature superposition rheology (Fig. 3c). The low-q region exhibited minimal changes, indicating an ultrastable microscale bicontinuous structure. The high-q region, corresponding to the nanoscale bicontinuous structure, remained stable below 40 °C, indicating that the ordered nanostructure was stable at both normal and high frequencies. Only above 40 °C, where chain dynamics of the PPFHEA-rich phase are activated (T_g≈34.3 °C), did the secondary interchain spacing peak (q≈3.4 nm^{-1}) diminish and the primary correlation peak (q≈2.0 nm^{-1}) broaden, indicating loss of structural order. These observations highlight the stability of the hierarchical bicontinuous structure over a wide temperature and frequency range.

Temperature-variable infrared (IR) spectra were collected from –20 °C to 80 °C to probe the internal physical interactions (Fig. 3d). Binary intensity changes in the ν(C=O) peak indicated the heat-induced weakening of dipolar interactions among PPFHEA ester groups and dissociation of hydrogen bonds among PAA carboxylic acid groups.[44] Binary changes were also observed for $\delta(H_2O)$ (O—H bending), suggesting the dissociation of hydrogen bonds between water and PAA

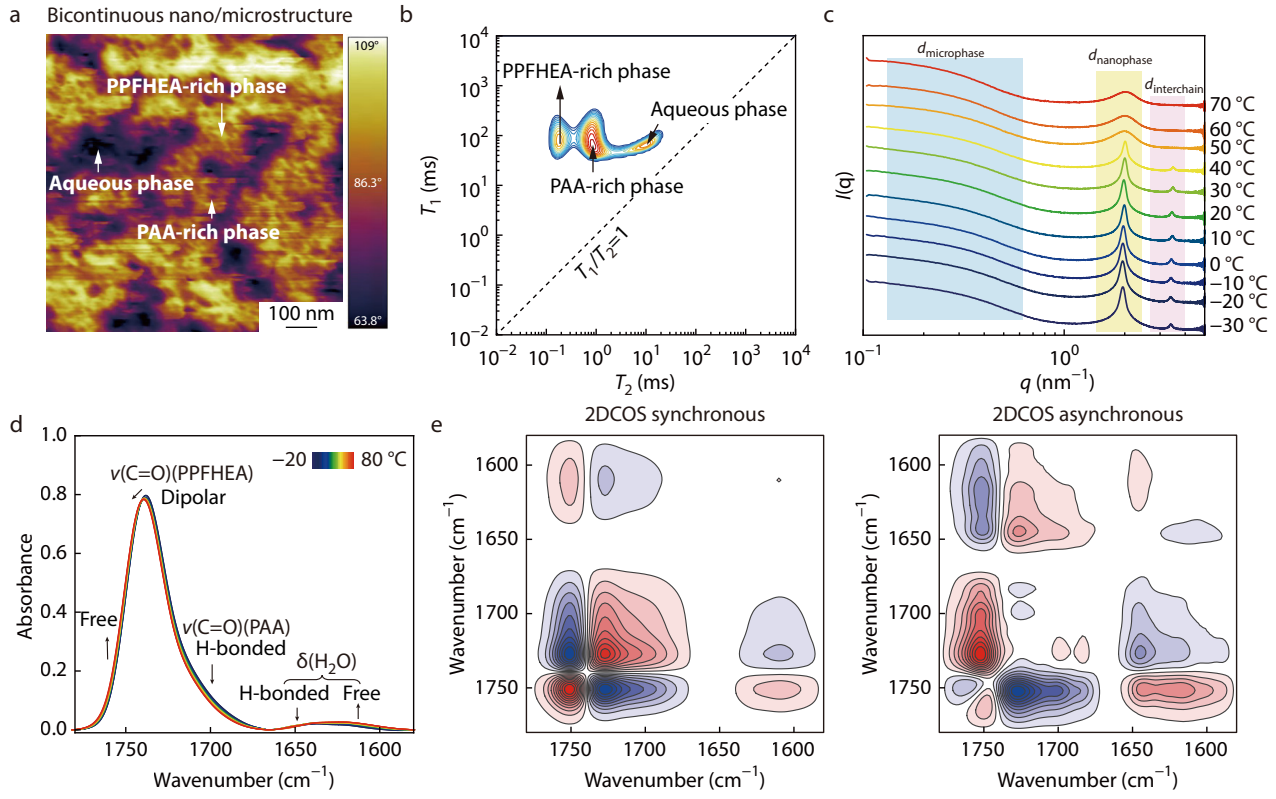

Fig. 3 Dynamic phase separation and physical interactions of P(PFHEA-*co*-AA$_{30\%}$) hierarchical hydrogel. (a) AFM phase image at 20 °C (lighter regions correspond to the PPFHEA-rich phase while darker regions to the PAA-rich and aqueous phases); (b) 2D low-field ^{1}H-NMR spectrum at 20 °C; (c) Temperature-variable SAXS profiles in log-log scale from −30 °C to 70 °C; (d) Temperature-variable IR spectra from −20 °C to 80 °C; (e) 2DCOS synchronous and asynchronous spectra derived from (d). Red and blue colors in 2DCOS spectra represent positive and negative intensities, respectively.

groups. Two-dimensional correlation spectroscopy (2DCOS) provided further insights into subtle interaction changes (Fig. 3e). Synchronous and asynchronous spectra reveal detailed information on intensity variations at specific wavenumbers.[48] According to Noda's rule,[44,49] the sequence of spectral responses was: 1645 cm^{-1} → 1610 cm^{-1} → 1684 cm^{-1} → 1699 cm^{-1} → 1728 cm^{-1} → 1753 cm^{-1} → 1765 cm^{-1} (→ denotes "prior to" or "earlier than"; see Table S1 for determination details in ESI). This sequence corresponds to δ(OH) (H_2O, H-bonded to PAA) → δ(OH) (free H_2O) → ν(C=O) (PAA, oligomeric H-bond) → ν(C=O) (PAA, dimeric H-bond) → ν(C=O) (PPFHEA, dipolar) → ν(C=O) (PAA, free) → ν(C=O) (PPFHEA, free). The earliest response of the PAA- and water-related groups indicates that heat-induced chain dynamics are driven by molecular changes in the PAA-rich hydrophilic phase. This confirms that the damping properties were dominated by the relaxation of the PAA-rich phase, which occurred at lower temperatures and higher frequencies. The subsequent response of the PPFHEA-related groups demonstrates the relative inertness of the PPFHEA-rich hydrophobic phase to temperature changes, which helps maintain a stable bicontinuous structure.

Underwater Acoustic Damping Properties

With advances in deep-sea exploration and marine engineering, underwater sound-absorbing materials are facing increasingly stringent performance requirements. In addition to optical transparency for unimpeded visual reconnaissance, an ideal material should reduce both transmitted and reflected sounds to avoid detection by active and passive sonars (Fig. 4a). Acoustic impedance matching with water is crucial for minimizing reflection at the material-water interface. Water has an acoustic impedance of approximately 1.45 MRayl. While the PAAm hydrogel with high water content showed a slightly higher impedance (1.6 MRayl), pure elastomers such as PDMS and PPFHEA with low sound velocities had much lower acoustic impedances (1.07 and 1.1 MRayl, respectively), which indicates high sound reflection at the elastomer-water interface (Fig. 4b). Crucially, the P(PFHEA-*co*-AA) hierarchical hydrogel achieved an acoustic impedance of 1.40 MRayl, which was remarkably close to that of water. This suggests that the presence of the PAA-rich phase effectively counteracts the low acoustic impedance of the PPFHEA-rich phase, resulting in a significantly enhanced and optimized acoustic impedance for minimal underwater sound reflection.

The high viscoelasticity and mechanical damping properties of the hierarchical hydrogel contributed to its high acoustic damping capacity, which significantly reduced the transmitted sound. The sound absorption coefficients (defined as the ratio of absorbed to incident sound intensity) were calculated using the transfer function method.[7] All four polymer materials with a thickness of 4 mm reached a plateau in the sound absorption coefficient at high frequencies (10^4–10^9 Hz) (Fig. 4c, Fig. S19 in ESI), which covers the frequency range of

common sonar and ultrasonic systems. Remarkably, the hierarchical hydrogel exhibited the highest acoustic damping capacity, with an average sound absorption coefficient of 0.78 (means 78% sound energy is absorbed). This performance is among the best reported for underwater sound absorbing materials (see Table S2 for a detailed comparison in ESI). While direct benchmarking is inherently constrained by variations in the frequency range, sample thickness, and measurement methodology, it is generally observed that the absorption coefficient correlates positively with thickness. An increased thickness extends the wave propagation paths and interaction time with the dissipative medium. Consequently, achieving high absorption in thin profiles places a greater demand on intrinsic energy dissipation mechanisms. Although some existing materials reach coefficients of 0.7–0.9, they typically require thicknesses exceeding 8 mm. In contrast, our hierarchical design enhanced the intrinsic dissipation efficiency, enabling significant acoustic attenuation without relying on the bulk material thickness.

To demonstrate the acoustic damping performance, we generated underwater sound waves at 500, 5000, and 20000 Hz (Fig. 4d; see the experimental setup in Fig. S20 in ESI). Compared to sound transmission in pure water, all four polymer materials attenuated the sound. The sound transmission loss, defined as $20\times\lg(V_0/V)$ in dB (where V and V_0 are the sound-induced electrical waveform amplitudes across the sample and water, respectively), was calculated (Fig. 4e).[50] All the samples showed increased transmission loss with frequency, which is consistent with the frequency-dependent damping figure of merits in Fig. 2(e). Due to its matched

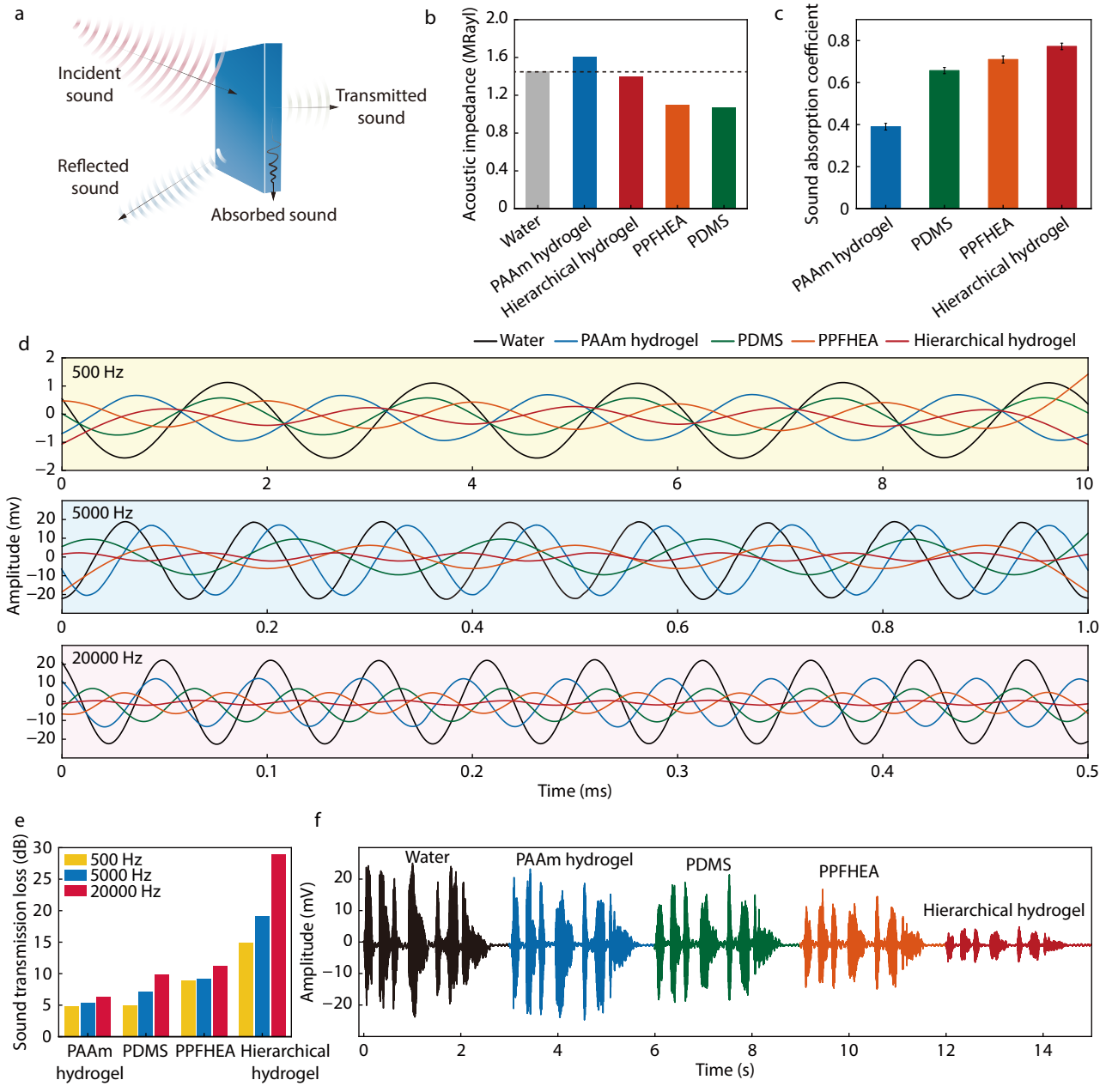

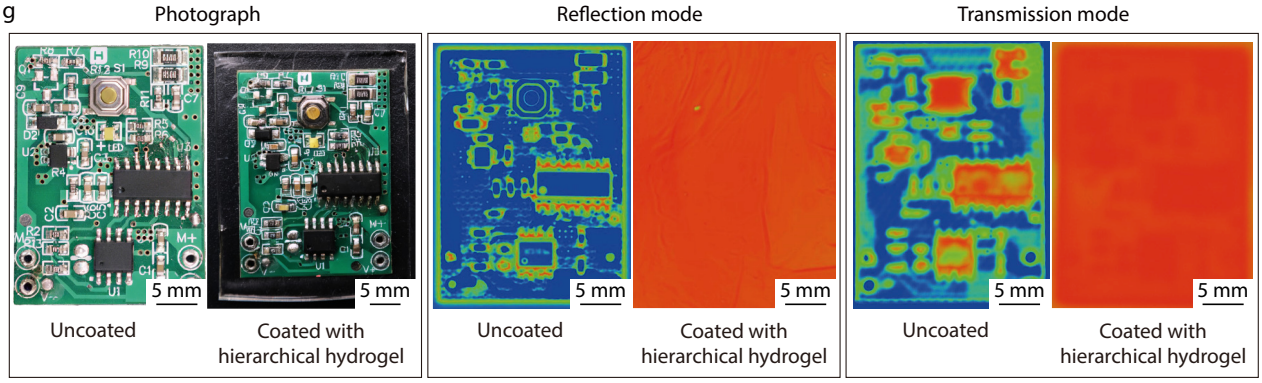

Fig. 4 Acoustic damping properties of P(PFHEA-*co*-$AA_{30\%}$) hierarchical hydrogel. (a) Schematic sound absorption, reflection, and transmission; (b) Acoustic impedances of water, PAAm hydrogel, PDMS, PPFHEA, and P(PFHEA-*co*-AA) hierarchical hydrogel; (c) Average sound absorption coefficients in the frequency range 10^4–10^9 Hz; (d) Simulated sound waves at 500, 5000, and 20000 Hz transmitted through water and different samples; (e) Corresponding sound transmission losses at different frequencies; (f) Acoustic damping of real sound waves; (g) Photographs and scanning acoustic microscopy images of a PCB with and without hierarchical hydrogel coating in reflection and transmission modes. Sample thickness for (c–g) is 4 mm.

impedance with water and high absorption coefficient, the hierarchical hydrogel exhibited the highest transmission loss. We further evaluated the damping performance by using real sound waves with complex waveforms. As shown in Fig. 4(f), the hierarchical hydrogel effectively dampened the real sound waves, whereas the control samples only slightly attenuated and distorted the waves.

Finally, scanning acoustic microscopy was used to demonstrate the acoustic attenuation capability of the hierarchical hydrogel as a coating (Fig. 4g). A printed circuit board (PCB) served as the target object. The C-scan technique clearly identified the PCB underwater in both reflection and transmission modes at 10 MHz. However, when coated with a transparent hierarchical hydrogel film (about 4 mm thick), nearly all the echo and transmitted signals were blocked, rendering the PCB acoustically invisible. These results underscore the potential of our hierarchical hydrogel for acoustic absorption applications such as camouflaging underwater robots and drones.

CONCLUSIONS

In this study, we developed a nanoconfined phase-separated P(PFHEA-*co*-AA) hierarchical hydrogel that combined optical transparency with acoustic damping. Unlike conventional homogeneous elastomers and hydrogels, our material featured a dual-scale bicontinuous structure with intertwined PPFHEA-rich, PAA-rich, and aqueous phases. This unique structure provides simultaneous acoustic impedance matching with water and a high viscoelasticity for attenuating vibrational energy. As a result, the hierarchical hydrogel maximized the incidence and absorption of broadband sound waves, significantly reducing reflection and transmission across a broad frequency range. The shape adaptability, optical camouflage, and acoustic attenuation make the hydrogel a promising coating material for underwater vehicles, devices, and robots. Furthermore, this nanoconfined hierarchical design strategy offers a new paradigm for developing advanced underwater soft materials with tunable optoacoustic properties.

Conflict of Interests

The authors declare no interest conflict.

Electronic Supplementary Information

Electronic supplementary information (ESI) is available free of charge in the online version of this article at http://doi.org/10.1007/s10118-026-3642-5.

Data Availability Statement

The related data of this paper is data that should not be shared, and can be obtained from the author for reasonable reasons. The author's contact information: shengtongsun@dhu.edu.cn.

ACKNOWLEDGMENTS

This work was financially supported by the National Natural Science Foundation of China (Nos. 52322306, 22275032, and 52433003) and Shanghai Oriental Talent Program.

REFERENCES

1 Li, Z.; Chitre, M.; Stojanovic, M. Underwater acoustic communications. *Nat. Rev. Electr. Eng.* **2025**, *2*, 83–95.
2 Li, G.; Wong, T. W.; Shih, B.; Guo, C.; Wang, L.; Liu, J.; Wang, T.; Liu, X.; Yan, J.; Wu, B.; Yu, F.; Chen, Y.; Liang, Y.; Xue, Y.; Wang, C.; He, S.; Wen, L.; Tolley, M. T.; Zhang, A. M.; Laschi, C.; Li, T. Bioinspired soft robots for deep-sea exploration. *Nat. Commun.* **2023**, *14*, 7097.
3 Gao, Y.; Song, J.; Li, S.; Elowsky, C.; Zhou, Y.; Ducharme, S.; Chen, Y. M.; Zhou, Q.; Tan, L. Hydrogel microphones for stealthy underwater listening. *Nat. Commun.* **2016**, *7*, 12316.
4 Yu, Z.; Wu, P. Underwater communication and optical camouflage ionogels. *Adv. Mater.* **2021**, *33*, 2008479.
5 Yuk, H.; Lin, S.; Ma, C.; Takaffoli, M.; Fang, N. X.; Zhao, X. Hydraulic hydrogel actuators and robots optically and sonically camouflaged in water. *Nat. Commun.* **2017**, *8*, 14230.
6 Zhang, Z.; Zhao, Y.; Gao, N. Recent study progress of underwater

Graphical Abstract

A Transparent Acoustic Damping Hydrogel with Dual-scale Bicontinuous Microphase Separation

Chen-Chen Lou, Bao-Hu Wu, Sheng-Tong Sun, and Pei-Yi Wu

Donghua University, China; Jülich Centre for Neutron Science (JCNS) at Heinz Maier-Leibnitz Zentrum (MLZ) Forschungszentrum Jülich, Germany

This work presents a hierarchical hydrogel that combines optical transparency and acoustic damping capacity. The hydrogel features a dual-scale bicontinuous nanostructure comprising three intertwined phases: hydrophilic, hydrophobic, and aqueous. This architecture enables acoustic impedance matching with water, strong vibrational damping, and ultrahigh absorption of sound.

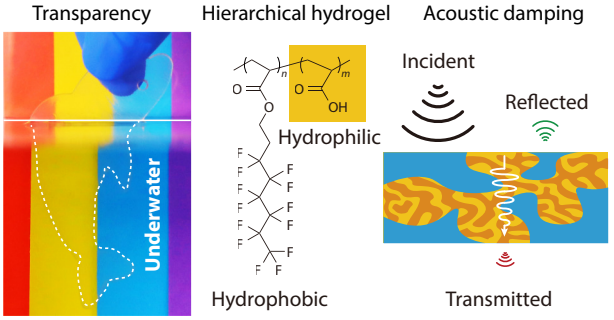

Chinese J. Polym. Sci. 2026, 44, 1727–1737 *https://doi.org/10.1007/s10118-026-3642-5*

sound absorption coating. *Eng. Rep.* **2023**, *5*, e12627.
7 Fu, Y.; Kabir, I. I.; Yeoh, G. H.; Peng, Z. A review on polymer-based materials for underwater sound absorption. *Polym. Test.* **2021**, *96*, 107115.
8 Dong, E.; Cao, P.; Zhang, J.; Zhang, S.; Fang, N. X.; Zhang, Y. Underwater acoustic metamaterials. *Natl. Sci. Rev.* **2022**, *10*, nwac246.
9 Gu, J.; Yan, S.; Zhang, L.; Su, C.; Yin, B.; Qu, S. Superior underwater sound-absorbing metasurface based on wave mode conversion and cavity-plate coupling resonance. *Compos. Struct.* **2023**, *323*, 117459.
10 Li, K.; Zhou, Z.; Huang, Z.; Lin, Y.; Chen, M.; Yang, P.; Li, Y. Underwater sound absorption characteristic of the rubber core sandwich structure with funnel-shaped cavities reinforced by carbon fiber columns. *Appl. Acoust.* **2023**, *208*, 109375.
11 Ma, F.; Wang, C.; Du, Y.; Zhu, Z.; Wu, J. H. Enhancing of broadband sound absorption through soft matter. *Mater. Horiz.* **2022**, *9*, 653–662.
12 Qu, S.; Gao, N.; Tinel, A.; Morvan, B.; Romero-García, V.; Groby, J.-P.; Sheng, P. Underwater metamaterial absorber with impedance-matched composite. *Sci. Adv.* **2022**, *8*, eabm4206.
13 Wang, B.; Qiao, C.; Wang, Y. l.; Dong, X.; Zhang, W.; Lu, Y.; Yuan, J.; Zeng, H.; Wang, H. Multifunctional underwater adhesive film enabled by a single-component poly(ionic liquid). *ACS Nano* **2023**, *17*, 5871–5879.
14 Zheng, J.; Luo, H.; Du, J.; Sun, S.; Cheng, Q.; Zhang, L.; Wang, D.; Wang, Y.; Zhou, H. Smart skin of underwater vehicle with dual functions of sound detection and absorption. *Nano Energy* **2024**, *129*, 110053.
15 Rossing, T. D., in *Springer handbook of acoustics*, Springer Science & Business Media, New York, **2007**, p. 1.
16 Sperling, L. H., in *Sound and vibration damping with polymers*, American Chemical Society, Washington, **1990**, p. 5.
17 Huang, J.; Zhou, H.; Zhang, L.; Zhang, L.; Shi, W.; Yang, Y.; Zhou, J.; Zhao, T.; Liu, M. Full-scale polymer relaxation induced by single-chain confinement enhances mechanical stability of nanocomposites. *Nat. Commun.* **2024**, *15*, 6747.
18 Zhang, J.; Zhou, N.; Dong, E.; Zhang, C.; Song, Z.; Liu, S.; Yang, C.; Su, X.; Wang, S.; Zhang, Y. Soft bio-metamaterials with high acoustic transparency and gradient refractive index for tunable acoustic beamformer. *Matter* **2024**, *7*, 3857–3875.
19 Zhang, K.; Ma, C.; He, Q.; Lin, S.; Chen, Y.; Zhang, Y.; Fang, N. X.; Zhao, X. Metagel with broadband tunable acoustic properties over air–water–solid ranges. *Adv. Funct. Mater.* **2019**, *29*, 1903699.
20 Dong, E.; Song, Z.; Zhang, Y.; Ghaffari Mosanenzadeh, S.; He, Q.; Zhao, X.; Fang, N. X. Bioinspired metagel with broadband tunable impedance matching. *Sci. Adv.* **2020**, *6*, eabb3641.
21 Zhao, X.; Zhou, Y.; Li, A.; Xu, J.; Karjagi, S.; Hahm, E.; Rulloda, L.; Li, J.; Hollister, J.; Kavehpour, P.; Chen, J. A self-filtering liquid acoustic sensor for voice recognition. *Nat. Electron.* **2024**, *7*, 924–932.
22 Tang, H.; Yang, Y.; Liu, Z.; Li, W.; Zhang, Y.; Huang, Y.; Kang, T.; Yu, Y.; Li, N.; Tian, Y.; Liu, X.; Cheng, Y.; Yin, Z.; Jiang, X.; Chen, X.; Zang, J. Injectable ultrasonic sensor for wireless monitoring of intracranial signals. *Nature* **2024**, *630*, 84–90.
23 Zhang, J.; Zhang, T.; Dong, E.; Zhang, C.; Lin, Z.; Song, Z.; Li, H.; Fang, N. X.; Zhang, Y. Bioinspired hydrogel jellyfish with mechanical flexibility and acoustic transparency. *Cell Rep. Phys. Sci.* **2022**, *3*, 101081.
24 Xu, Y.; Tan, J.; Dong, W.; Chen, Y.; Wuliu, Y.; Xu, W.; Wang, R.; Yin, G.; Zhang, Z.; Zhu, C.; Xu, J.; Tian, L. Super strong and tough hydrogels constructed *via* network uniformization of macromolecular chains. *Adv. Funct. Mater.* **2025**, *35*, 2419161.
25 Jiang, L.; Li, F.; Li, Y.; Pi, M.; Xie, J.; Zhang, J.; Guo, H.; Ran, R.; Cui, W. Solvent-free fabrication of robust physical hdrogels *via* bulk copolymerization for underwater acoustics. *Adv. Mater.* **2025**, *37*, 2508162.
26 Göransson, P. Acoustic and vibrational damping in porous solids. *Phil. Trans. R. Soc. A* **2006**, *364*, 89–108.
27 Dong, J.; Tian, P. Review of underwater sound absorption materials. *IOP Conf. Ser.: Earth Environ. Sci* **2020**, *508*, 012182.
28 Kim, J.; Zhang, G.; Shi, M.; Suo, Z. Fracture, fatigue, and friction of polymers in which entanglements greatly outnumber cross-links. *Science* **2021**, *374*, 212–216.
29 Zhang, C.; Bao, Q.; Zhu, H.; Zhang, Q. Highly transparent and long-term stable dielectric elastomer composites enabled by poly(ionic liquid) inclusion. *Adv. Funct. Mater.* **2024**, *34*, 2401901.

30 Groh, W.; Zimmermann, A. What is the lowest refractive index of an organic polymer. *Macromolecules* **1991,** *24*, 6660–6663.
31 Humzah, M. D. Tyndall, Rayleigh, Mei, and Raman scattering: Understanding their role in aesthetics. *J. Cosmet. Dermatol.* **2024**, *23*, 3493–3496.
32 Chen, G.; Wu, J.; Wang, Z.; Zhu, H.; Zhu, S.; Zhang, Q. Armored polymer-fluid gels with integrated damping and impact protection across broad temperatures. *Sci. Adv.* **2025**, *11*, eadv5292.
33 Xiang, H.; Li, X.; Wu, B.; Sun, S.; Wu, P. Highly damping and self-healable ionic elastomer from dynamic phase separation of sticky fluorinated polymers. *Adv. Mater.* **2023**, *35*, 2209581.
34 Xu, Z.; Lu, J.; Lu, D.; Li, Y.; Lei, H.; Chen, B.; Li, W.; Xue, B.; Cao, Y.; Wang, W. Rapidly damping hydrogels engineered through molecular friction. *Nat. Commun.* **2024**, *15*, 4895.
35 Zhang, Y.; Yuan, J.; Hu, J.; Tian, Z.; Feng, W.; Yan, H. Toward understanding the cross-linking from molecular chains to aggregates by engineering terminals of supramolecular hyperbranched polysiloxane. *Aggregate* **2024**, *5*, e404.
36 Shi, Y.; Wu, B.; Sun, S.; Wu, P. Peeling–stiffening self-Adhesive ionogel with superhigh interfacial toughness. *Adv. Mater.* **2024**, *36*, 2310576.
37 Wang, Y. C.; Ludwigson, M.; Lakes, R. S. Deformation of extreme viscoelastic metals and composites. *Mat. Sci. Eng. A* **2004**, *370*, 41–49.
38 Zhang, P.; To, A. Highly enhanced damping figure of merit in biomimetic hierarchical staggered composites. *J. Appl. Mech.* **2014**, *81*, 051015.
39 Park, B.; Shin, J. H.; Ok, J.; Park, S.; Jung, W.; Jeong, C.; Choy, S.; Jo, Y. J.; Kim, T.-i. Cuticular pad–inspired selective frequency damper for nearly dynamic noise–free bioelectronics. *Science* **2022**, *376*, 624–629.
40 Lakes, R. *Viscoelastic Materials*. Cambridge University Press **2009**.
41 Wu, Y.; Wang, Y.; Guan, X.; Zhang, H.; Guo, R.; Cui, C.; Wu, D.; Cheng, Y.; Ge, Z.; Zheng, Y.; Zhang, Y. Molecular clogging organogels with excellent solvent maintenance, adjustable modulus, and advanced mechanics for impact protection. *Adv. Mater.* **2023**, *35*, 2306882.
42 Grindy, S. C.; Learsch, R.; Mozhdehi, D.; Cheng, J.; Barrett, D. G.; Guan, Z.; Messersmith, P. B.; Holten-Andersen, N. Control of hierarchical polymer mechanics with bioinspired metal-coordination dynamics. *Nat. Mater.* **2015**, *14*, 1210–1216.
43 Qiao, H.; Wu, B.; Sun, S.; Wu, P. Entropy-driven design of highly impact-stiffening supramolecular polymer networks with salt-bridge hydrogen bonds. *J. Am. Chem. Soc.* **2024**, *146*, 7533–7542.
44 Li, X.; Wu, B.; Sun, S.; Wu, P. Making sticky-slippery switchable fluorogels through self-adaptive bicontinuous phase separation. *Adv. Mater.* **2024**, *36*, 2411273.
45 Song, Y. Q.; Kausik, R. NMR application in unconventional shale reservoirs—a new porous media research frontier. *Prog. Nucl. Magn. Reson. Spectrosc.* **2019,** *112–113*, 17–33.
46 Wang, S.; Zhang, L.; Wang, Z.; Song, Z.; Liu, H.; Tian, Z.; Xu, X. Humidity-adaptive, mechanically robust, and recyclable bioplastic films amplified by nanoconfined assembly. *Aggregate* **2024**, *5*, e643.
47 Huang, J.; Xu, Y.; Qi, S.; Zhou, J.; Shi, W.; Zhao, T.; Liu, M. Ultrahigh energy-dissipation elastomers by precisely tailoring the relaxation of confined polymer fluids. *Nat. Commun.* **2021**, *12*, 3610.
48 Hou, L.; Wu, P.; Sun, S. Physical interaction-driven design of modulus-adaptive polymers. *Sci. China Mater.* **2025**, *68*, 3526.
49 Li, L.; Wu, B.; Sun, S.; Wu, P. High-entropy thermal-stiffening hydrogels with fast switching dynamics. *Natl. Sci. Rev.* **2025**, *12*, nwaf072.
50 Zeqiri, B.; Scholl, W.; Robinson, S. P. Measurement and testing of the acoustic properties of materials: a review. *Metrologia* **2010**, *47*, S156.

https://doi.org/10.1007/s10118-026-3642-5